

Article

Pyrolyzed Bacterial Cellulose as the Backbone of the Cathode Catalyst-CoFe₂O₄ for the Li-O₂ Battery

Xiangjun Wang ^{1,*}, Yongqing Chi ¹, Peng Wu ²  and Wen Liu ¹

¹ School of Chemical and Biological Engineering, Taiyuan University of Science and Technology, Taiyuan 030024, China

² Computer Engineering Department, Taiyuan Institute of Technology, Taiyuan 030008, China

* Correspondence: wangxiangjun@tyust.edu.cn

Abstract: In this paper, CoFe₂O₄@pyrolyzed bacterial cellulose (CFO@PBC) nanocomposites were synthesized by a hydrothermal process and an in situ composite technique as the cathode for rechargeable Li-O₂ batteries (LOB). CoFe₂O₄@Ketjenblack (CFO@KB) were prepared in the same way as the comparison. The as-prepared materials were characterized by SEM, XRD, and BET. The LOB with CFO@PBC-3 showed a maximum initial discharge capacity of 2660 mAh g⁻¹ (electrode) at the current density of 100 mA g⁻¹, while the mass ratio of CoFe₂O₄ and pyrolyzed bacterial cellulose was 3. The cyclic voltammetry of the CFO@PBC nanocomposite electrodes was investigated at 0.1 mVs⁻¹ in the voltage window of 2.0–4.5 V. With the limited capacity of 640 mAh g⁻¹ (electrode), the CFO@PBC-3 electrode showed the best cycle stability and higher cutoff voltage of discharging. The pyrolyzed bacterial cellulose, as the fibrous 3D backbone in CFO@PBC nanocomposite electrodes, produced better results than the CFO@KB.

Keywords: pyrolyzed bacterial cellulose; LOB; cutoff voltage; voltage gap



Citation: Wang, X.; Chi, Y.; Wu, P.; Liu, W. Pyrolyzed Bacterial Cellulose as the Backbone of the Cathode Catalyst-CoFe₂O₄ for the Li-O₂ Battery. *Crystals* **2022**, *12*, 1165. <https://doi.org/10.3390/cryst12081165>

Academic Editor: Yutaka Moritomo

Received: 21 July 2022

Accepted: 13 August 2022

Published: 19 August 2022

Publisher's Note: MDPI stays neutral with regard to jurisdictional claims in published maps and institutional affiliations.



Copyright: © 2022 by the authors. Licensee MDPI, Basel, Switzerland. This article is an open access article distributed under the terms and conditions of the Creative Commons Attribution (CC BY) license (<https://creativecommons.org/licenses/by/4.0/>).

1. Introduction

Due to the high theoretical capacity and wide potential window, lithium–oxygen batteries (LOB) have attracted great attention as one of the most promising power sources for electric vehicles and portable devices [1]. Electrocatalytic oxygen reduction reaction (ORR) and oxygen evolution reaction (OER) play critical roles in the development of LOB [2]. The slow kinetics of the ORR and the OER at the cathode determine the power energy density, energy efficiency, and voltage efficiency with a voltage gap larger than 1.0 V [3]. Rare metal materials are known to be the most active electrocatalysts for the ORR, as platinum-based materials. However, the high cost, scarcity, and moderate activity of the OER of Pt hinder the application of LOB [4]. Substantial efforts have been dedicated to alternative non-noble metal catalysts, especially spinel oxides, which have attracted greater attention due to the high catalytic activities toward ORR and OER [5].

Recently, the bifunctional electrocatalyst, spinel CoFe₂O₄ combined with carbon materials has been reported, such as monodispersed porous CoFe₂O₄ (CFO) nanospheres on graphene [4], CoFe₂O₄/Carbon Nanotubes Hybrid, CoFe₂O₄@multi-walled carbon nanotubes, and 3D hierporous spinel CoFe₂O₄ hollow nanospheres [6]. CoFe₂O₄ has been confirmed to show good electrocatalytic for OER and ORR. However, the conductivity of spinel CoFe₂O₄ should also be enhanced to increase efficiency. Thus, the addition of a conductive substrate would benefit spinel CoFe₂O₄ to increase its performance. Pyrolyzed Bacterial Cellulose (PBC) has attracted increasing attention as the electrode material in batteries and supercapacitors due to its excellent conductivity, three-dimensional network, and high specific surface area [7–11]. Moreover, bacterial cellulose (BC), the specific product of the primary metabolism of plant biomass, could be cultured easily and in large quantities by the bacteria of genera *Acetobacter*. Thus, BC is an economic, environmentally friendly,

and petroleum-replacing choice, in addition to its good performance. PBC, as a derive of the bacterial cellulose, retains these advantages of bacterial cellulose, compared with other carbon materials.

Herein, CFO@PBC samples, synthesized by a hydrothermal process and an in situ composite technique, as an efficient bifunctional electrocatalyst for ORR and OER in rechargeable LOBs were studied in this work. Their characteristics were tested by XRD, SEM, and BET. The electrochemical performances, such as the initial discharge capacity, cyclic voltammetry, and limited-capacity cycling were investigated. Because Ketjenblack (KB) was regarded as a candidate for electrode material due to its excellent conductivity and high specific surface area [12–14], CFO@KB was tested for comparison.

2. Materials and Methods

PBC was prepared according to a previous paper [8]. Then, the PBC was treated with nitric acid at 120 °C for 3 h to obtain the PBC oxide (OPBC). Then, 10mg OPBC was dispersed in 50 mL of anhydrous ethanol to obtain the OPBC suspension. Next, 0.2 M $\text{Fe}(\text{NO}_3)_3 \cdot 9\text{H}_2\text{O}$ and 0.2 M $\text{Co}(\text{NO}_3)_2 \cdot 6\text{H}_2\text{O}$ ($\geq 99.0\%$, Guoyao Chemical Reagent Co., Ltd., Taiyuan, China) were added to the above PBC suspension with different weight ratios of CoFe_2O_4 ($\geq 99.0\%$, Guoyao Chemical Reagent Co., Ltd., Taiyuan, China) and PBC (1:1, 3:1, 5:1, 7:1), following 10 h stirring at room temperature. Then, 2.5 mL NH_4OH (28%, Guoyao Chemical Reagent Co., Ltd., Taiyuan, China) at room temperature was added to the mixture and heated at 80 °C for 12 h. Next, the mixture was transferred to 50 mL Teflon autoclaves for hydrothermal treatment at 150 °C for 3 h. After the reactor was cooled to room temperature, the precipitate was filtered with a funnel and washed with ethanol and deionized water to remove any impurities. The final product was obtained after drying at 60 °C 12 h. The samples obtained were abbreviated to CFO@PBC-1, CFO@PBC-3, CFO@PBC-5, and CFO@PBC-7 according to the weight ratios. (Figure 1) The same strategy was employed to prepare CFO@KB-1, CFO@KB-3, CFO@KB-5, and CFO@KB-7 with KB (Lion Corporation, EC-600JD, add Taiyuan, China).

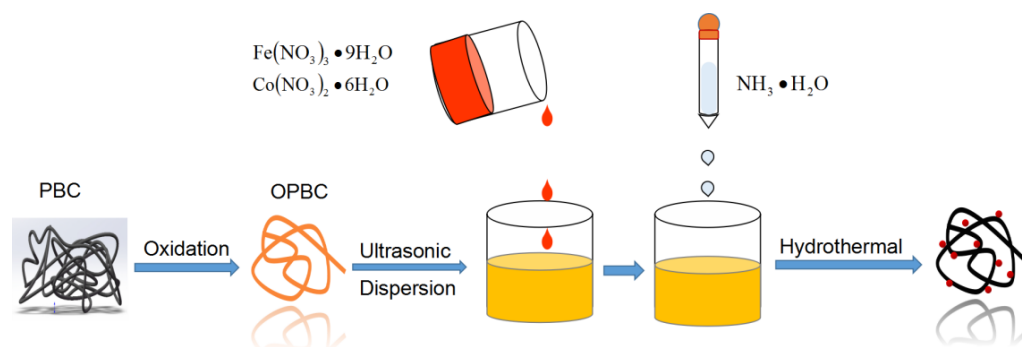


Figure 1. Preparation of the CFO@PBC samples.

The crystal structures of the CFO@PBC and CFO@KB samples were examined with X-ray diffraction (XRD) using a Bede D1 X-ray diffractometer (Cu K α radiation; operated at 40 kV, 45 mA; $\lambda = 0.15418$ nm; Bede Scientific Ltd.; Durham, UK); the diffraction angle ranged from 10° to 80° with a step of 0.02° and a rate of 1.2° min^{-1} . The samples were tested by SEM using a GeminiSEM 300 (Zeiss, Thuringia, Germany). The nitrogen adsorption was measured using a Micromeritics accelerated surface area porosimetry (ASAP 2020, USA) auto adsorption analyzer to obtain N_2 adsorption isotherms at 77 K, and the specific surface area (SSA) of the CFO@PBC samples was obtained by Brunauer–Emmett–Teller (BET) analyses of the adsorption isotherms.

The CFO@PBC- and CFO@KB- based cathode catalysts were prepared separately by mixing the active material with a polyvinylidene fluoride (PVDF) binder in N-methyl-2-pyrrolidone (NMP) and carbon black at a weight ratio of 80:10:10 and cast on current collectors. The cell assembly was carried out in an argon-filled glovebox with lithium

foil as the counter electrode, porous polypropylene film, Celgard 2325, as the separator, and 1 M trifluoromethane lithium in Tetraethyleneglycol dimethyl ether (TEGDME) as the electrolyte in 2032-type coin cells. Galvanostatic discharge–charge tests were performed using a CT2001A battery program controlling the test system with a current of 100 mA g^{-1} . Cyclic voltammetry (CV) measurements were carried out at a scan rate of 0.1 mV s^{-1} between 2 V and 4.5 V using the CHI 1000C Electrochemical measurement system.

3. Results

Figure 2a shows the XRD patterns of the PBC and CFO@PBC samples. As shown, the main peak of PBC around 22.5° had an obvious wide-beat shoulder peak, instead of a sharp peak, assigned to the (002) plane, with defective crystalline areas and non-crystalline areas. The XRD patterns of CFO@PBC-1 showed the characteristic peaks of 2θ at 19.3° , 30.3° , 33.3° , 36.5° , and 41.9° , which were well-matched peaks with the (111), (220), (311), (222), and (400) crystal surface of the JCPDS standard card, respectively. The intensity of the peaks gradually increased as the weight ratios increased, with CFO@PBC-7 being the highest. This indicated that the CFO was well introduced to the PBC [15].

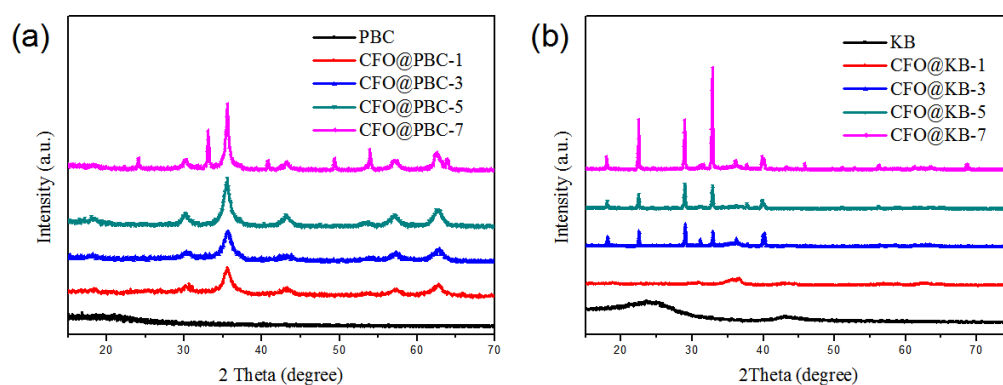


Figure 2. XRD patterns of (a) PBC and CFO@PBC samples; (b) KB and CFO@KB samples.

Figure 2b shows the XRD patterns of the KB and CFO@KB samples. As shown, the main peak of KB around 24° had an obvious wide-beat shoulder peak, on behalf of the classic amorphous carbon smoky quartz stone type diffraction peak. Another peak at 40.2° showed the characteristics of a diffraction peak, which was representative of the typical amorphous region of carbon. The XRD patterns of the CFO@KB samples showed similar characteristics.

Figure 3 shows the SEM images of the PBC, CFO@KB, and CFO@PBC. The PBC exhibited interconnected fibrous morphology with a diameter under $1 \mu\text{m}$ (Figure 3a). After the hydrothermal process, the CFO as circled in red was gradually coated on the surface of the PBC. The fibrous morphology of the PBC was maintained. The surface of the obtained CFO@PBC was rough, and the diameter was around $2 \mu\text{m}$ (Figure 3c,d). However, the CFO@KB without the fibrous morphology of the PBC showed a disordered stacking of CFO on the surface of the KB (Figure 3b).

The hydrothermal method for the assembly of CFO onto PBC effectively reduced the specific surface areas (SSA) and the quantity of the micropores. The specific surface areas measured in accordance with the standard BET method were $337 \text{ m}^2\text{g}^{-1}$, $181 \text{ m}^2\text{g}^{-1}$, $161 \text{ m}^2\text{g}^{-1}$, $105 \text{ m}^2\text{g}^{-1}$, and $81 \text{ m}^2\text{g}^{-1}$, respectively for PBC, CFO@PBC-1, CFO@PBC-3, CFO@PBC-5, and CFO@PBC-7. Figure 4 depicts the BET nitrogen adsorption–desorption isotherm of the PBC and CFO@PBC samples at 77 K. The PBC represented a type IV isotherm with H4 type hysteresis loop, while the CFO@PBC samples showed a type IV isotherm. The hysteresis loop in the P/P0 range of $\sim 0.6\text{--}1.0$ was indicative of mesoporosity in addition to the presence of microporosity. Although the SSA of the CFO@PBC samples decreased with the increase in the CFO, CFO@PBC-3 had the highest microporosity ratio.

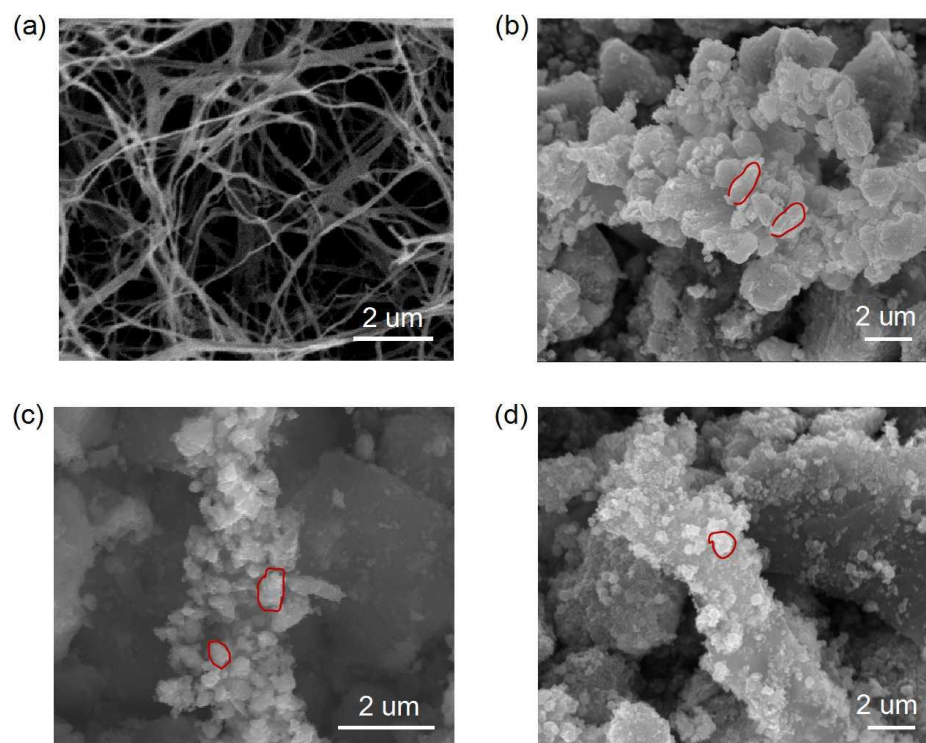


Figure 3. SEM images of (a) PBC, (b) CFO@KB, and (c,d) CFO@PBC.

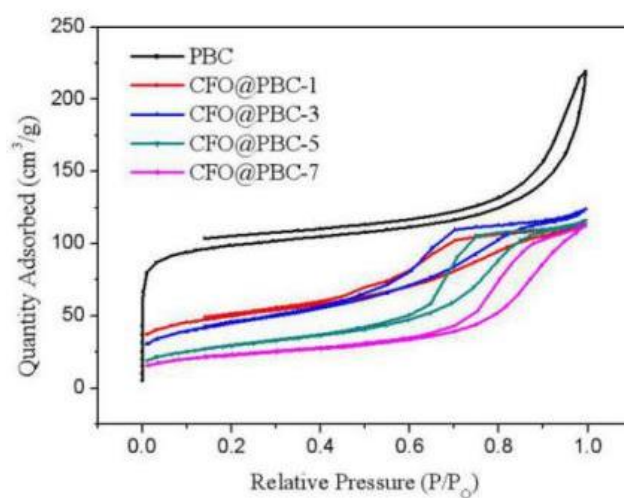


Figure 4. Nitrogen adsorption–desorption isotherm of the PBC and CFO@PBC samples.

4. Discussion

The electrochemical processes of oxygen in the Li-O₂ cell were investigated using cyclic voltammetry (CV). Figure 5a shows the CV curves of CFO@KB-1 from 2.0 to 4.5 V at a constant scan rate of 0.1 mVs⁻¹. There was one peak (2.0–2.5 V) in the discharge process and one peak (4.0–4.5 V) in the charging process, which was consistent with the formation and decomposition of Li₂O₂. Figure 5b shows the initial discharge curves of the Li-O₂ cells with different CFO@PBC samples incorporating the oxygen electrodes loaded with a voltage range from 2.7 V to 2.37 V. The initial discharge capacities were successively 801 mAh·g⁻¹, 2660 mAh·g⁻¹, 603 mAh·g⁻¹, and 564 mAh·g⁻¹ for CFO@PBC-1, CFO@PBC-3, CFO@PBC-5, and CFO@PBC-7 respectively. The Li-O₂ cells with CFO@PBC-3 had the best performance.

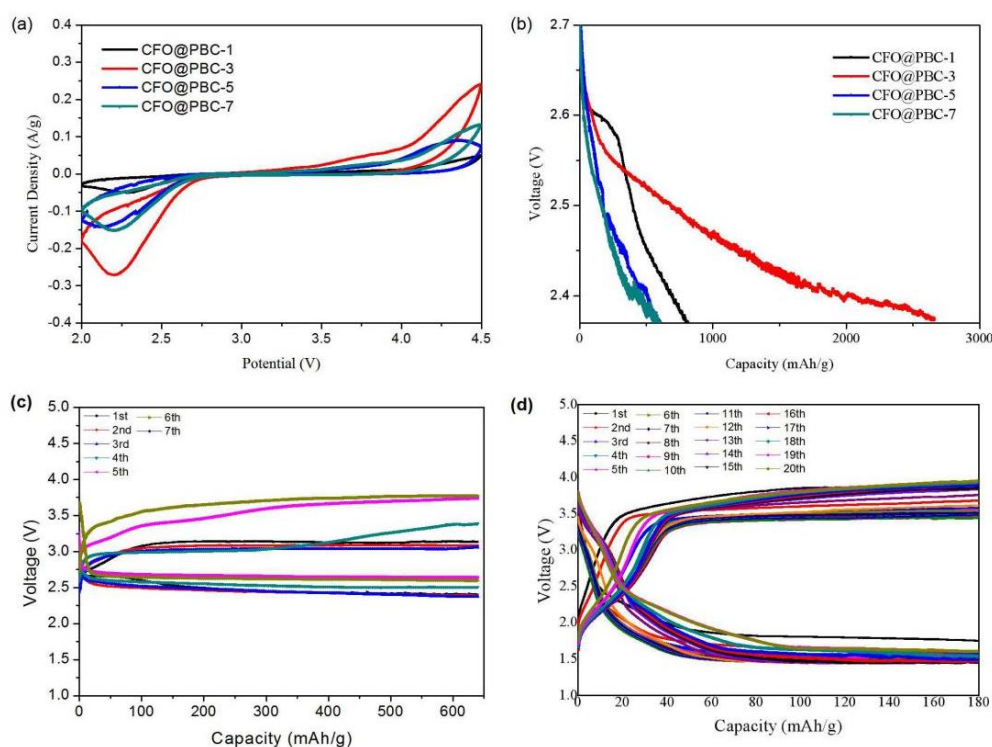


Figure 5. (a) CV curves of Li-O₂ cells with different CFO@PBC samples at 0.1 mVs⁻¹; (b) initial discharge curves of Li-O₂ cells with different CFO@PBC samples at a current density of 100 mA g⁻¹; (c) limited capacitance cycling of Li-O₂ cells with CFO@PBC-3 samples with 640 mAh g⁻¹; (d) limited capacitance cycling of Li-O₂ cells with CFO@KB-3 with 180 mAh g⁻¹.

Li₂O₂ was the major discharge product employed by Raman spectroscopy and XRD [16,17], while there would also be partial formation of Li₂O₂ through the oxygen consumption measurements [18]. Many studies [19–21] suggest that the formation of the Li₂O₂ is not direct, but formed with the intermediate, LiO₂. [22]



The reduction of O₂ to O₂⁻ usually occurs in the presence of a catalyst. Reactions (1)–(3) present a general mechanism wherein the reduction is rate-limited by a one-electron transfer to O₂ to form a superoxide (O₂⁻, LiO₂). When LiO₂ is formed in the electrolyte, equilibrium is reached between the LiO₂ adsorbed on the cathode surface and the LiO₂ dissolved in the electrolyte. Thus, the solubility of LiO₂ in electrolytes is a key factor affecting the kinetics of the discharge process. Enough space in the hosting cathode was required for the efficient redox reaction.

Figure 5b shows the initial discharge curves of the Li-O₂ cells with different CFO@PBC samples at a current density of 100 mA g⁻¹. The initial discharge capacity of Li-O₂ cells with CFO@PBC-3 exceeded that of the other CFO@PBC samples, which was due to the high microporosity ratio of CFO@PBC. Initial discharge curves of Li-O₂ cells with different CFO@KB samples at a current density of 100 mA g⁻¹ were shown in Figure S1. The voltage gaps between the charging voltage and discharging voltage were tested following the capacity-limited cycle method. Figure 5c shows the first seven cycles of the LOB with CFO@PBC-3 with a limited capacity of 640 mAh g⁻¹ (electrode). Figure S2 shows the first 20 limited-capacity cycles of the Li-O₂ batteries with CFO@KB-1. The voltages of the charging platforms for the first five cycles were around 3 V, while the discharging

platforms were above 2.37 V. The voltage gaps were less than 0.7 V for the first five cycles and 1.5 V for the sixth and seventh cycles. Figure 5d shows the first 20 cycles of the LOB with CFO@KB-3 with a limited capacity of $180 \text{ mAh}\cdot\text{g}^{-1}$ (electrode). The voltages of the charging platforms were around 3.5 V, while the discharging platforms were about 1.5 V. The voltage gaps were 2 V. Figure S3 shows the voltage gap and cutoff voltage for the first 20 limited-capacity cycles of the Li-O₂ batteries with CFO@KB samples. For LOB, the cutoff voltage with a capacity-limited cycle method was the prescribed lower-limit voltage at which battery discharge capacity was considered at the limited value. The cutoff voltage highly depended on the whole capacity the battery possessed. With cycling, the cutoff voltage of the LOB with CFO@PBC-3 increased to nearly 2.6 V, which was the theoretical discharge stage, whereas the cutoff voltage of the LOB with CFO@KB decreased to 1.5 V. This indicated that the intermediate product, LiO₂, was accumulated and thicker, as the solid electrolyte interphase (SEI) film was formed. These results show that PBC is the better backbone for CFO in Li-O₂ batteries compared with KB, due to its 3D nanostructure.

5. Conclusions

In conclusion, the electrocatalytic catalyst, CFO, was synthesized with different proportions of PBC and KB and tested in Li-O₂ cells. The results showed that the CFO@PBC-3 had the best capacity and cycle stability, which benefitted from the suitable size CFO grain with a weight ratio of 1:3 and the fibrous backbone of PBC. The LOB with the CFO@PBC-3 electrode showed an initial discharge capacity of 2660 mAhg^{-1} (electrode), while the capacities decreased with the increase in the weight ratios of the CFO. The limited-capacity cycling curves of the LOB showed that the CFO@PBC-3 had better stability with the capacity and higher cutoff voltages. In the future, more biomaterials-based carbon should be studied as the backbone of the electrocatalytic catalyst in Li-O₂ batteries.

Supplementary Materials: The following are available online at <https://www.mdpi.com/article/10.3390/cryst12081165/s1>, Figure S1: Initial discharge curves of Li-O₂ cells with different CFO@KB samples at a current density of $100 \text{ mA}\cdot\text{g}^{-1}$, Figure S2: The first 20 limited-capacity cycles of the Li-O₂ batteries with CFO@KB-1 (a), CFO@KB-3 (b), CFO@KB-5 (c), and CFO@KB-7 (d), Figure S3: The voltage gap (a) and cutoff voltage (b) for the first 20 limited-capacity cycles of the Li-O₂ batteries with CFO@KB samples.

Author Contributions: Conceptualization, X.W. and P.W.; Investigation, Y.C.; writing—review and editing, W.L. All authors have read and agreed to the published version of the manuscript.

Funding: This research was funded by Shanxi Province Foundation Science for Youths, grant number 201701D221067.

Institutional Review Board Statement: Not applicable.

Informed Consent Statement: Not applicable.

Data Availability Statement: Not applicable.

Conflicts of Interest: The authors declare no conflict of interest.

References

1. Lei, X.; Liu, B.; Koudakan, P.A.; Pan, H.; Qian, Y.; Wang, G. Single-atom catalyst cathodes for lithium–oxygen batteries: A review. *Nano Futures* **2022**, *6*, 012002. [[CrossRef](#)]
2. Zhang, J.; Chen, X.; Lei, Y.; Lu, H.; Xu, J.; Wang, S.; Yan, M.; Xiao, F.; Xu, J. Highly rechargeable lithium oxygen batteries cathode based on boron and nitrogen co-doped holey graphene. *Chem. Eng. J.* **2022**, *428*, 131025. [[CrossRef](#)]
3. Wang, L.; Deng, J.; Lou, Z.; Zhang, T. Cross-linked p-type Co₃O₄ octahedral nanoparticles in 1D n-type TiO₂ nanofibers for high-performance sensing devices. *J. Mater. Chem. A* **2014**, *2*, 10022–10028. [[CrossRef](#)]
4. Yan, W.; Cao, X.; Ke, K.; Tian, J.; Jin, C.; Yang, R. One-pot synthesis of monodispersed porous CoFe₂O₄ nanospheres on graphene as an efficient electrocatalyst for oxygen reduction and evolution reactions. *RSC Adv.* **2016**, *6*, 307–313. [[CrossRef](#)]
5. Yang, S.T.; Wu, Z.; Xie, J.; Liao, R.; Zhang, X.; Yu, B.; Wu, R.; Liu, X.; Li, H.; Guo, Z. Fe₃O₄@SiO₂ nanoparticles as high-performance Fenton-like catalyst in neutral environment. *RSC Adv.* **2016**, *5*, 5458–5463. [[CrossRef](#)]

6. Xu, Y.; Bian, W.; Wu, J.; Tian, J.H.; Yang, R. Preparation and electrocatalytic activity of 3D hierarchical porous spinel CoFe_2O_4 hollow nanospheres as efficient catalyst for Oxygen Reduction Reaction and Oxygen Evolution Reaction. *Electrochim. Acta* **2015**, *151*, 276–283. [[CrossRef](#)]
7. Wang, Y.; Wang, Y.; Jiang, L. Freestanding carbon aerogels produced from bacterial cellulose and its $\text{Ni}/\text{MnO}_2/\text{Ni}(\text{OH})_2$ decoration for supercapacitor electrodes. *J. Appl. Electrochem.* **2018**, *48*, 495–507. [[CrossRef](#)]
8. Wang, X.; Kong, D.; Zhang, Y.; Wang, B.; Li, X.; Qiu, T.; Song, Q.; Ning, J.; Song, Y.; Zhi, L. All-biomaterial supercapacitor derived from bacterial cellulose. *Nanoscale* **2016**, *8*, 9146–9150. [[CrossRef](#)]
9. Liang, H.W.; Wu, Z.Y.; Chen, L.F.; Li, C.; Yu, S.H. Bacterial cellulose derived nitrogen-doped carbon nanofiber aerogel: An efficient metal-free oxygen reduction electrocatalyst for zinc-air battery. *Nano Energy* **2015**, *11*, 366–376. [[CrossRef](#)]
10. Wang, X.; Kong, D.; Wang, B.; Song, Y.; Zhi, L. Activated pyrolysed bacterial cellulose as electrodes for supercapacitors. *Sci. China-Chem.* **2016**, *59*, 713–718. [[CrossRef](#)]
11. Yang, H.; Li, Y.; Long, P.; Han, J.; Cao, C.; Yao, F.; Feng, W. Amorphous red phosphorus incorporated with pyrolyzed bacterial cellulose as a free-standing anode for high-performance lithium ion batteries. *RSC Adv.* **2018**, *8*, 17325–17333. [[CrossRef](#)] [[PubMed](#)]
12. Li, Y.; Wang, L.; He, X.; Tang, B.; Jin, Y.; Wang, J. Boron-doped Ketjenblack based high performances cathode for rechargeable $\text{Li}-\text{O}_2$ batteries. *J. Energy Chem.* **2016**, *25*, 131. [[CrossRef](#)]
13. Li, J.; Zhou, Z.; Liu, K.; Li, F.; Peng, Z.; Tang, Y.; Wang, H. $\text{Co}_3\text{O}_4/\text{Co}-\text{N}-\text{C}$ modified ketjenblack carbon as an advanced electrocatalyst for Al-air batteries. *J. Power Sources* **2017**, *343*, 30–38. [[CrossRef](#)]
14. Tashima, D.; Yoshitama, H.; Otsubo, M.; Maeno, S.; Nagasawa, Y. Evaluation of electric double layer capacitor using Ketjenblack as conductive nanofiller. *Electrochim. Acta* **2011**, *56*, 8941–8946. [[CrossRef](#)]
15. Narsimulu, D.; Padmaraj, O.; Srinadhu, E.S.; Satyanarayana, N. Synthesis, characterization and electrical properties of mesoporous nanocrystalline CoFe_2O_4 as a negative electrode material for lithium battery applications. *J. Mater. Sci. Mater. Electron.* **2017**, *28*, 17208–17214. [[CrossRef](#)]
16. Ogasawara, T.; Débart, A.; Holzapfel, M.; Novák, P.; Bruce, P.G. Rechargeable Li_2O_2 Electrode for Lithium Batteries. *J. Am. Chem. Soc.* **2006**, *128*, 1390. [[CrossRef](#)]
17. McCloskey, B.D.; Bethune, D.S.; Shelby, R.M.; Girishkumar, G.; Luntz, A.C. Solvents' Critical Role in Nonaqueous Lithium–Oxygen Battery Electrochemistry. *J. Phys. Chem. Lett.* **2011**, *2*, 1161–1166. [[CrossRef](#)] [[PubMed](#)]
18. Liu, C.; Brant, W.R.; Younesi, R.; Dong, Y.; Edström, K.; Gustafsson, T.; Zhu, J. Towards an understanding of Li_2O_2 evolution in $\text{Li}-\text{O}_2$ batteries: An in Operando synchrotron X-ray diffraction study. *ChemSusChem* **2017**, *10*, 1592–1599. [[CrossRef](#)]
19. Guéguen, A.; Novák, P.; Berg, J. XPS Study of the Interface Evolution of Carbonaceous Electrodes for $\text{Li}-\text{O}_2$ Batteries during the 1st Cycle. *J. Electrochem. Soc.* **2016**, *163*, A2545–A2550. [[CrossRef](#)]
20. Gallant, B.M.; Kwabi, D.G.; Mitchell, R.R.; Zhou, J.; Thompson, C.V.; Shao-Horn, Y. Influence of Li_2O_2 morphology on oxygen reduction and evolution kinetics in $\text{Li}-\text{O}_2$ batteries. *Energy Environ. Sci.* **2013**, *6*, 2518–2528. [[CrossRef](#)]
21. Younesi, R.; Hahlin, M.; Björefors, F.; Johansson, P.; Edström, K. $\text{Li}-\text{O}_2$ Battery Degradation by Lithium Peroxide (Li_2O_2): A Model Study. *Chem. Mater.* **2013**, *25*, 77–84. [[CrossRef](#)]
22. Hou, J.; Jie, X.; Graetz, J.; Ellis, M.W.; Uosaki, K. Electrochemistry of rechargeable lithium-air batteries. In *Rechargeable Lithium Batteries*; Woodhead Publishing: Cambridge, UK, 2015; pp. 149–181.